

Highly Sensitive and Wearable Liquid Metal-Based Pressure Sensor for Health Monitoring Applications: Integration of a 3D-Printed Microbump Array with the Microchannel

Kyuyoung Kim, Jungrak Choi, Yongrok Jeong, Incheol Cho, Minseong Kim, Seunghwan Kim, Yongsuk Oh,* and Inkyu Park*

Wearable pressure sensors capable of sensitive, precise, and continuous measurement of physiological and physical signals have great potential for the monitoring of health status and the early diagnosis of diseases. This work introduces a 3D-printed rigid microbump-integrated liquid metal-based soft pressure sensor (3D-BLiPS) for wearable and health-monitoring applications. Using a 3D-printed master mold based on multimaterial fused deposition modeling, the fabrication of a liquid metal microchannel and the integration of a rigid microbump array above the microchannel are achieved in a one-step, direct process. The microbump array enhances the sensitivity of the pressure sensor (0.158 kPa^{-1}) by locally concentrating the deformation of the microchannel with negligible hysteresis and a stable signal response under cyclic loading. The 3D-BLiPS also demonstrates excellent robustness to 10 000 cycles of multidirectional stretching/bending, changes in temperature, and immersion in water. Finally, these characteristics are suitable for a wide range of applications in health monitoring systems, including a wristband for the continuous monitoring of the epidermal pulse rate for cuffless blood pressure estimation and a wireless wearable device for the monitoring of body pressure using a multiple pressure sensor array for the prevention of pressure ulcers.

1. Introduction


Soft pressure sensors have received significant research attention in a variety of fields, including soft robotics, electronic skin, and wearable electronics. Wearable soft pressure sensors have great potential for the real-time monitoring of health status and for the early diagnosis of disease. As a major component of soft electronic devices, a soft pressure sensor is required to have high compliance, high sensitivity, low cost,

long-term stability in performance, and environmental stability in order for it to be employed in continuous health monitoring. Solid-state devices using various types of functional materials, such as graphene,^[1] carbon nanotubes,^[2] and carbon black,^[3] have been utilized as soft pressure sensors with micro/nano patterned elastomers.^[4] However, these solid-state pressure sensors suffer from limited stretchability, signal drifting, and long-term instability due to the differences in the mechanical properties between the functional materials and flexible substrates. Furthermore, they have exhibited high sensitivity to environmental conditions (e.g., temperature and moisture), limiting their use in wearable and continuous health monitoring applications. Recently, to overcome these issues, liquid-state electronics using ionic liquids^[5] or liquid metals^[6] have been introduced for wearable applications. Of these materials, Galinstan, a eutectic metal alloy of gallium, indium, and tin, has exhibited significant promise for use in wearable and health monitoring applications due to its high electrical conductivity ($3.4 \times 10^6 \text{ S m}^{-1}$), negligible vapor pressure at room temperature, self-healing properties, unlimited reversible strain range, and nontoxicity.^[7] Previous studies have proposed liquid metal-based pressure sensors that utilize multilayer capacitive microfluidic channels,^[8] embedded solid particles,^[9] and diaphragm micropumps.^[6c,10] However, it is difficult to monitor sub-kPa pressures due to the limited sensitivity of liquid metal-based pressure sensors with robust signal recovery in health monitoring applications.^[11]

In the present study, we introduce a 3D-printed rigid microbump array-integrated liquid metal-based soft pressure sensor (3D-BLiPS). With the help of 3D printing using multimaterial fused deposition modeling (FDM), a liquid metal microchannel was fabricated by sacrificing a water-soluble microchannel master mold with the simultaneous monolithic integration of a 3D-printed rigid microbump array above the microchannel, significantly reducing the complexity of the manufacturing process for the microchannel and allowing functional structures to be embedded with precise alignment. In addition, all the materials used in our sensor are nontoxic or biocompatible for

K. Kim, J. Choi, Y. Jeong, I. Cho, M. Kim, S. Kim, Dr. Y. Oh, Prof. I. Park
Department of Mechanical Engineering
Korea Advanced Institute of Science and Technology
291 Daehak-ro, Yuseong-gu, Daejeon 34141, Republic of Korea
E-mail: oyongsuk@kaist.ac.kr; inkyu@kaist.ac.kr

Dr. Y. Oh
Center for Bio-Integrated Electronics
Simpson Querrey Institute for Nano/Biotechnology
Northwestern University
Evanston, IL 60208, USA

 The ORCID identification number(s) for the author(s) of this article can be found under <https://doi.org/10.1002/adhm.201900978>.

DOI: 10.1002/adhm.201900978

human, which is an essential for its applications in healthcare. The 3D-printed microbump array, fabricated using simple and cost-effective FDM 3D printing, enhances the pressure sensitivity ($0.158 \text{ kPa}^{-1}@50 \text{ kPa}$) by locally concentrating the deformation of the microchannel with negligible hysteresis, a stable signal response, and high signal recovery characteristics. The 3D-BLiPS also demonstrates excellent mechanical and physicochemical stability when exposed to multidirectional cyclic stretching, variation in temperature, and immersion in water. To illustrate the use of the proposed pressure sensor in health monitoring applications, we produced a continuous epidermal pulse-monitoring wristband linked to an electrocardiogram (ECG) signal for the cuffless blood pressure estimation and a wireless wearable body pressure monitoring system using a

multiple pressure sensor array for the continuous tracking of changes in the pressure on the heel and ankle.

2. Results and Discussion

2.1. Design and Fabrication of the 3D-BLiPS

The 3D-BLiPS consists of four major components: a microchannel-patterned top layer, liquid metal, 3D-printed microbumps, and a bottom layer (Figure 1a). The top and the bottom layers are fabricated using the stretchable elastomer Dragon Skin 10, which has an extremely high stretchability (1000%) and a low elastic modulus ($E = 150 \text{ kPa}$ for $\epsilon = 100\%$). These

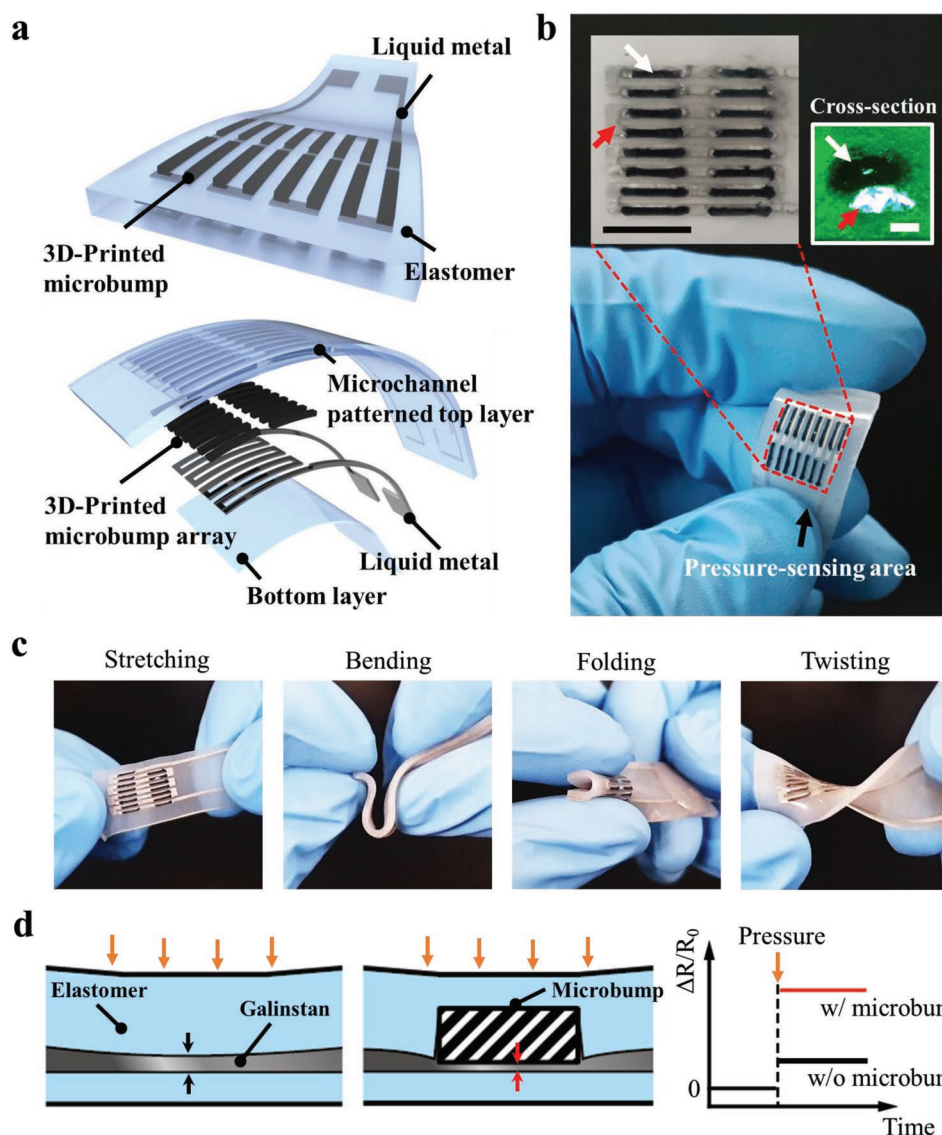


Figure 1. a) Schematic view of the proposed 3D-printed rigid microbump-integrated liquid metal-based pressure sensor (3D-BLiPS). b) Images of the 3D-BLiPS. Inset (red dashed lines) shows a magnified image of the pressure-sensing area (scale bar = 5 mm). The other inset shows a cross-section of the microchannel. The white and red arrows indicate the embedded rigid microbump and liquid metal, respectively (scale bar = 200 μm). c) Images of the 3D-BLiPS under various forms of mechanical deformations: stretching, bending, folding, and twisting. d) Effect of the microbump on pressure sensitivity.

characteristics are suitable for the substrate as well as the encapsulation layer for the prevention of liquid metal leakage in stretchable electronics applications. Following this, a multilayered structure of polyvinyl alcohol (PVA), which acted as a sacrificial layer for the microchannel formation, and polylactic acid (PLA), used for the rigid microbump array, was fabricated using a multinozzle FDM 3D printing process. After the encapsulation of the multilayered structure, the PVA layer was selectively removed using water intrusion to produce the microchannel, while the 3D-printed rigid microbumps were monolithically integrated with the microchannel. The empty microchannel was then filled with Galinstan (Figure 1b). The liquid metal inside the microchannel was electrically connected with embedded electrical wires as interconnectors for the measurement of resistance. Details of the fabrication process are explained further in the Experimental Section (Figures S1 and S2, Supporting Information). Owing to its excellent mechanical properties, the fabricated sensor is capable of perfectly reversible stretching, bending, folding, and twisting (Figure 1c).

Generally, piezoresistive liquid metal-based pressure sensors measure pressure via the geometric deformation of the microchannel under an applied load. External pressure decreases the cross-sectional area of the microchannel and induces an increase in resistance along the microchannel. The pressure sensitivities of previously reported liquid metal-based pressure sensors were as low as $0.2\text{--}80 \times 10^{-3} \text{ kPa}^{-1}$, especially in the low-pressure range ($<50 \text{ kPa}$).^[8a,9a,10c,d,11a,12] Because the liquid metal is encapsulated in a soft elastomer with thick top layer, the applied pressure is distributed as the nearly incompressible elastomer, which has a Poisson's ratio of 0.499 and a low elastic modulus, expands perpendicular to the direction of the pressure. This results in a small geometrical change in the microchannel filled with liquid metal. According to previous studies, the response of the microchannel-based pressure sensor is affected by various components including Poisson's ratio of the material, top layer thickness, microchannel dimension, and so on.^[13] The smaller Poisson's ratio and the thinner top layer are preferred for higher pressure sensitivity (Figure S3, Supporting Information). However, rigid materials with smaller Poisson's ratio cannot provide the soft mechanical properties as the elastomer does. Also, when the thickness of the top layer is too small, below $100 \mu\text{m}$, for example, the mechanical stability of the microchannel may be decreased by bursting or tearing under high pressure in fabrication process or various applications. Therefore, we have integrated the rigid microbump array having a smaller Poisson's ratio at specific parts inside the elastomer with $200\text{--}250 \mu\text{m}$ of the top layer thickness. When rigid microbumps with an elastic modulus that is 20 000 times higher ($\approx 3.5 \text{ GPa}$) and Poisson's ratio of 0.35 are integrated into the microchannel, the ratio of the load transmitted from the surface to the microchannel is increased so that the external pressure leads to a significant reduction in the cross-sectional area of the microchannel (Figure 1d) by locally concentrating deformation below the microbumps. As a consequence, the sensor response to the applied pressure is greatly improved.

2.2. Pressure Sensing Performance

The sensing performance of the 3D-BLiPS was assessed in terms of normalized resistance change, the limit of detection, response time, and dynamic response. The experimental setup for the sensor characterization process is described in the Experimental Section and Figure S4 (Supporting Information). The change in the normalized resistance of the 3D-BLiPS was 5.8 times higher than that of a typical liquid metal-based pressure sensor without microbumps at a pressure of 50 kPa (Figure 2a). This observation was supported by finite element method simulation results, which revealed that the cross-sectional area reduces when rigid microbumps are integrated into the microchannel under the same applied pressure (Figure 2b; details about the simulation model are provided in Figure S5, Supporting Information).

The pressure sensor was capable of operating up to the pressure of 600 kPa before failure (Figure S6a, Supporting Information). Figure S6b,c (Supporting Information) illustrates the full loading and unloading cycles of the 3D-BLiPS and the uniformity of 12 different pressure sensors, respectively. Differences in the dimensions of the 3D-printed mold and the volume of liquid metal within the microchannel may have caused variation in sensing performance. This could be improved by 3D printing with higher precision and by removing the native oxide layer of the liquid metal prior to the filling process to lower the surface tension.^[7a]

In order to investigate the lower detection limit, we dropped small water droplets onto the pressure sensor (Figure 2c). Six consecutive drops produced a continuous increase in the response, and the removal of the water drops decreased the signal to the initial level. Each droplet had a weight of $27.3 \pm 0.4 \text{ mg}$, which corresponds to a pressure of $\approx 2.7 \text{ Pa}$. It is true that the intrinsic signal noise from the measurement setup and the environment could hinder the accurate estimation of the lower detection limit. Thus, we can assume that the lower detection limit of the sensor is below 16 Pa (i.e., the pressure of six water droplets) which corresponds to 5 of signal to noise ratio ($2H/h = 5$). In addition, mild air movement produced by a hand air blower could be detected, illustrating that weak noncontact stimuli could be detected by the proposed sensor (Figure 2d). The response time (τ), defined as the time required for the response to rise from 20% to 80% of the final value of the sensor, was 77 ms at the given step input (Figure 2e). The response time is dependent on the viscoelastic behavior of materials and the loading conditions. Generally, a smaller pressure loading leads to shorter response times due to less stress relaxation time. The 3D-BLiPS exhibited no signal drifting and perfectly reversible signals against dynamic loading at pressures below 25 kPa (Figure 2f). Our proposed sensor has the lowest limit of detection with enhanced sensitivity and broad sensing range among liquid metal-based pressure sensors developed to date, by the help of integrated rigid microbumps with the liquid microchannel. Also, the sensitivity, limit of detection, and response time of our sensor are comparable with those of common solid-state pressure sensors as summarized in Figure S10 and Table S2 in the Supporting Information.

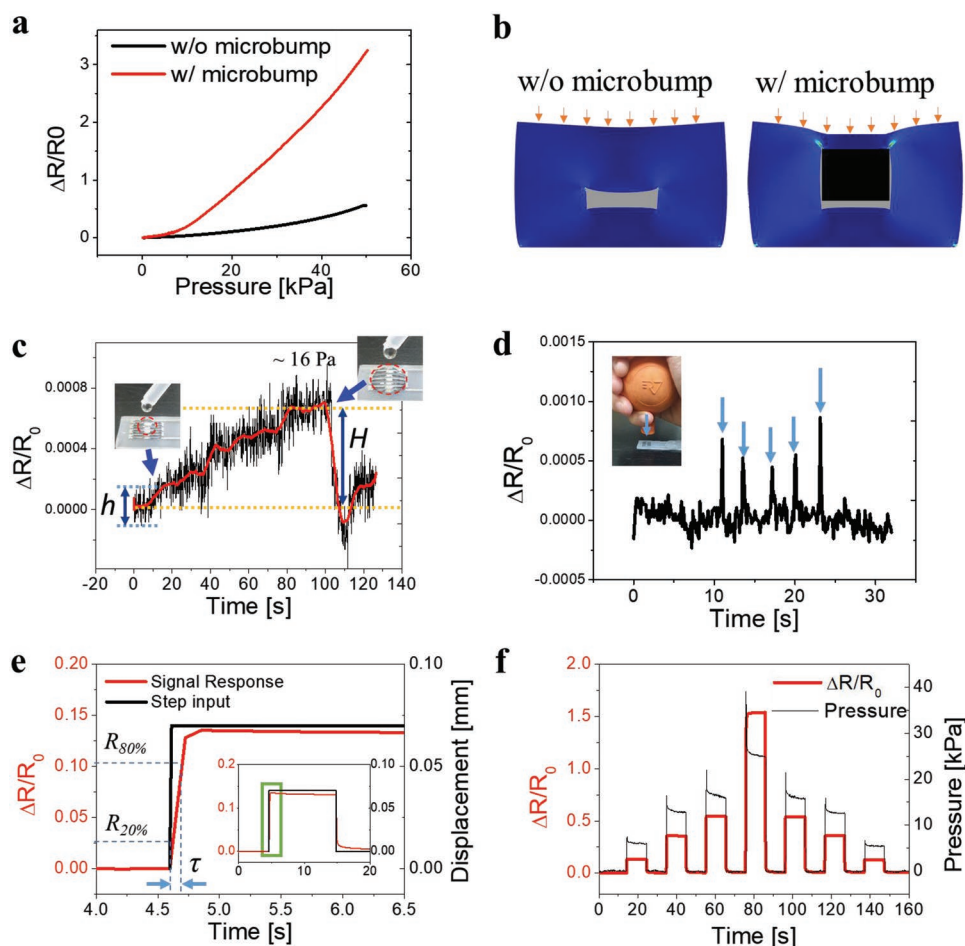


Figure 2. Sensing performance of the 3D-BLiPS. a) Response to the applied pressure for the sensors with and without rigid microbumps. b) Simulation results comparing the change in cross-sectional area under the same pressure between the sensors with and without the microbumps. c) Sensor response to water droplets. Six consecutive droplets were dropped onto the sensor (H , h : the magnitude of signal and noise, respectively). d) Sensor response to airflow. e) Step response and response time (τ) estimation for the sensor (Inset: overall signal response). f) Dynamic response of the sensor to the application of varying pressure levels.

2.3. Stability

It is important for the sensor to have excellent signal recovery characteristics to ensure stable performance and a long lifetime before failure. The 3D-BLiPS showed long-term stability and mechanical durability in response to 12 000 repeated cyclic loadings with a compressive pressure of 0–30 kPa (Figure 3a). Signal drifting and structural changes were not significant during the compression/release cycles due to the stable mechanical and electrical properties of the liquid metal and elastomer. By comparing the sensing performance for the 1st, 100th, 1000th, 5000th, and 10 000th cycles, we observed relatively constant pressure-sensing performance (Figure 3b). Long-term stability was also observed for cyclic loadings in lower (≈ 15 kPa) and higher pressure (≈ 45 kPa) ranges (Figure S6d,e, Supporting Information).

Wearable pressure sensors are subject to various forms of mechanical deformation, including multidirectional stretching and bending. Therefore, we compared the bending sensitivity of the sensor with and without microbumps. When these sensors were bent with a bending radius (ρ) between $\rho_0 = \infty$ mm

and $\rho_1 = 5$ mm, the relative resistance changed by a maximum of only 2.7% and 2.4%, respectively (Figure 3c). There were no significant changes in the responses to bending even with the presence of the microbump array, due to the mechanical separation between bottom and top layers and the advantages of the intrinsic material properties of liquid metal (Figure S5c,d, Supporting Information). In addition, 10 000 loading cycles were applied for bending radii from $\rho = 21.7$ to 5.9 mm. The signal returned to its initial value with negligible drifting (maximum change $< 0.3\%$), thus demonstrating excellent signal recovery and reliability (Figure 3d). In order to assess the stability of the sensor in response to tensile loading, 10 000 stretching cycles from $\varepsilon = 0\%$ to $\varepsilon = 20\%$ were applied along the x - and y -directions (Figure 3e,f). The resistance increased when strain in the x -direction was applied and decreased when strain in the y -direction was applied, following the general relationship between resistance and the geometrical parameters of the resistors. Due to the excellent recovery characteristics of the liquid metal, the sensor signal returned to its initial value with a small change (maximum change $< 3.0\%$) following stretching in both the x - and y -directions (Figure 3g). Minor drift occurred

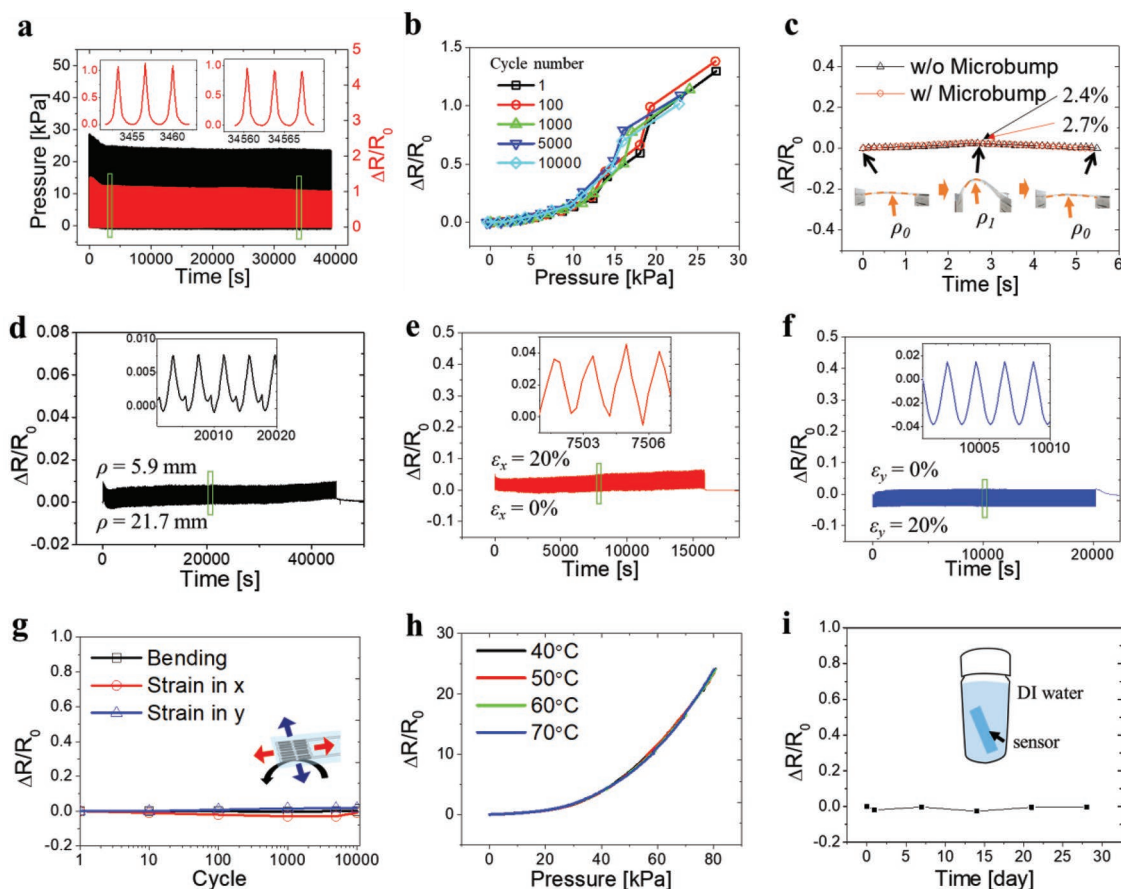


Figure 3. Stability analysis of the 3D-BLiPS. a) 12 000 cyclic loading with a compressive pressure below 30 kPa (Inset: signal response at 1000 and 10 000 cycles). b) Sensor response versus pressure after repeated loading of 1, 100, 1000, 5000, and 10 000 cycles. c) Change in the base resistance due to bending and unbending motions ($\rho_0 = \infty$ mm to $\rho_1 = 5$ mm) for the sensors with and without rigid microbumps. d) Response of the sensor during 10 000 bending cycles ($\rho = 21.7$ mm to $\rho = 5.9$ mm). e, f) Response of the sensor for 10 000 stretching cycles in the x- and y-directions ($\varepsilon = 0\%$ to $\varepsilon = 20\%$). g) Signal recovery during 10 000 cycles of bending and stretching in the x- and y-directions. h) Effect of temperature on sensor performance. i) Effect of moisture on the sensor.

in response to unidirectional strain, which may have been due to the viscoelastic behavior of the elastomer and the change in the loading conditions by the slipping of the sensor in the holding jig. The resistance change occurred by in-plane strain could be reduced by modifying the pattern of the microchannel to serpentine or wavy structures.^[14]

To investigate the effect of temperature on sensing performance, we applied pressure and measured the change in resistance at different temperatures (40, 50, 60, and 70 °C), as shown in Figure S8a,b (Supporting Information). Even though the initial resistance (R_0) increased as the temperature rose (Figure S8c, Supporting Information), the sensor response ($\Delta R/R_0$) to the pressure was constant for all temperatures (Figure 3h). Thus, it is possible to remove the temperature effect of the sensor using appropriate temperature compensation. In addition, the sensor showed a very stable resistance after water immersion over a period of 4 weeks (Figure 3e and Figure S8d, Supporting Information). This indicates that the sensor forms an effective seal with no leakage of liquid metal or infusion of water through the encapsulation package. We also conducted a self-heating test on the sensor for 24 h; its response remained almost the same even with a high current

of 580 mA (Figure S8e, Supporting Information). This thermal, chemical, and electrical stability of the 3D-BLiPS thus allows for robust sensing performance in daily wearable applications, such as health monitoring systems.

2.4. Application: Epidermal Pulse Monitoring System and Wireless Wearable Heel Pressure Monitoring System

The advantageous characteristics of the 3D-BLiPS, including its high sensitivity, excellent response speed, and high long-term stability, allows for its application in health monitoring systems. Here, we report on its use in two different healthcare applications: biosignal monitoring in the form of a wristband for measuring the epidermal pulse rate and blood pressure (BP), and human motion and posture monitoring in the form of a body pressure measurement system. The pulse rate and BP are vital health indicators that quantitatively evaluate the cardiovascular diseases and the general health, and their non-invasive and continuous measurement is required in various healthcare applications for prognosis and diagnosis purposes. Compared with cuff-based BP measurement, the pulse transit

time (PTT) method has gained in popularity due to its noninvasive, continuous, and convenient measurement without the need for a cuff.^[15] PTT is the time required for the arterial pulse to propagate from the heart to the body and it can be measured by the time interval between the wave peaks of an ECG and the epidermal pulse, achieved by either photoplethysmogram^[16] or wrist pressure sensors.^[17] According to previous studies on cuffless blood pressure estimation, systolic BP (SBP) and diastolic BP (DBP) can be measured using the PTT method.^[17b,18]

In the fabrication of a wristband integrated with the 3D-BLiPS and a measurement system (Figure S9, Supporting Information) for monitoring the epidermal pulse, the 3D-BLiPS was mounted on the wristband with the help of a rigid support to accurately position it above the blood vessel (Figure 4a). Figure 4b shows the epidermal pulse rate of two subjects during the experiment. Subject A and B performed 45 squats (i.e., standing up and down) for 45 s and took a rest for 5 min sitting on a chair. For Subject A, the pulse rate was between 70 and 80 beats per minute (bpm) at rest, and it increased rapidly during the exercise. At the end of the exercise, Subject A's epidermal pulse rate reached about 120 bpm, indicating that the exercise was high-intensity. During rest, the pulse rate recovered gradually to the initial pulse rate. Subject B exhibited a similar trend while having a lower pulse rate than Subject A. Figure 4c,d shows the pulse signals for Subject A at rest (Green circle) and during exercise (Red circle) for 10 s, respectively.

We can clearly observe that the frequency of the pulse increased after the exercise, with differences in the magnitude of the response noticeable, indicating that the strength of the pulse and the blood pressure level changed after exercise.

To measure the epidermal pulse and ECG signals simultaneously for PTT calculation and blood pressure estimation, we fabricated a wearable device by combining the 3D-BLiPS and a commercial ECG measurement module (Figure 4e). The epidermal pulse and ECG signals were continuously monitored during exercise (30 squats in 30 s), and the PTT was calculated before and after the exercise by measuring the time difference between the adjacent peaks of the epidermal pulse and the ECG signal. PTT₀ (normal state) and PTT₁ (exercise) were calculated to be 278 and 238 ms, respectively (Figure 4f,g). The decrease in the PTT indicates that the time required for the arterial pulse to travel from the heart to the wrist reduced, thus indicating a higher mean blood pressure in the blood vessels after exercise. The estimated SBP and DBP of Subject A were 138.4 ± 4.2 and 66.8 ± 1.4 mmHg, respectively, compared to 125 and 73 mmHg when measured using an automatic digital blood pressure monitor with a cuff. This proves that the 3D-BLiPS can be useful in a wearable, cuffless blood pressure monitoring system.

Body pressure monitoring is important for healthcare applications because it provides information about movement, body position, and locally concentrated pressure.^[19] Patients who cannot express themselves or move/control their body are at

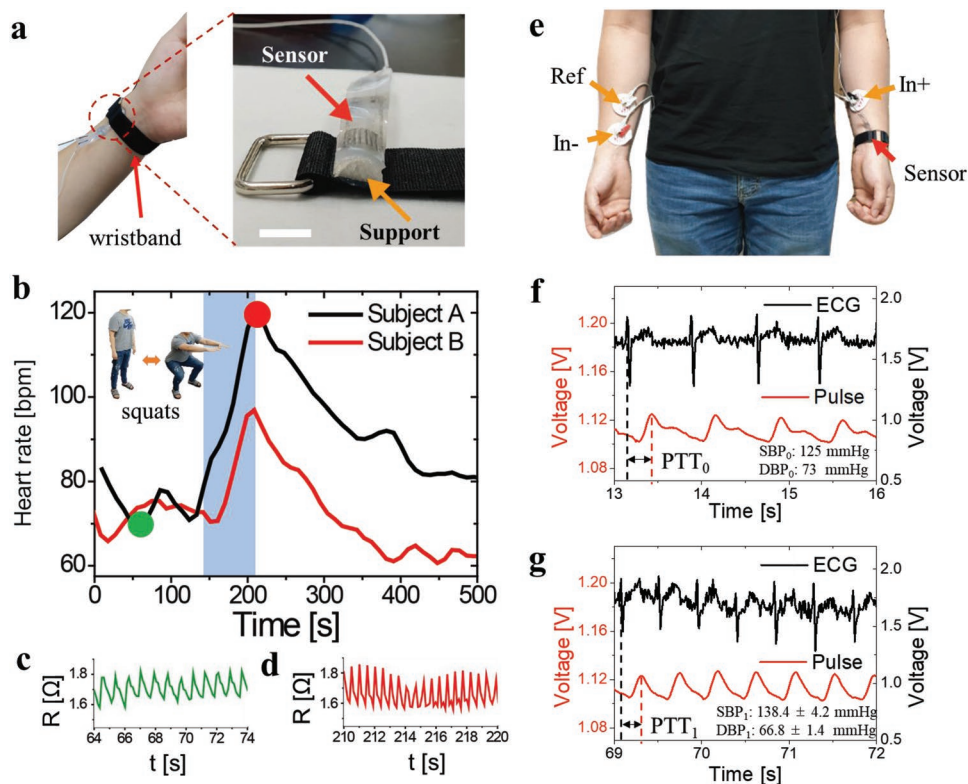


Figure 4. Health monitoring application of the 3D-BLiPS 1): Epidermal pulse rate monitoring and cuffless blood pressure estimation system. a) Images of the wearable wristband for epidermal pulse rate monitoring (scale bar = 10 mm). b) Pulse rate during the preparation, exercise, and rest periods. c,d) Continuous epidermal pulse before and after exercise, respectively. e) Cuffless blood pressure monitoring system using simultaneous ECG and epidermal pulse measurements. f,g) Continuous epidermal pulse and ECG signals for PTT calculation before and after exercise, respectively (PTT₀ = 278 ms (*n* = 7), PTT₁ = 238 ms (*n* = 10)). SBP and DBP were estimated to be 138.4 ± 4.2 and 66.8 ± 1.4 mmHg, respectively, after exercise.

risk of bedsores (also known as pressure ulcers), which occur over a bony prominence as a result of shearing, friction, prolonged pressure, or other environmental effects and which cause pain, discomfort, and secondary infections. It is known that a continuous pressure of 13 kPa on the skin for 6 h result in complete muscle necrosis and 9 kPa for 2 h in pathologic change.^[20] To prevent bedsores, continuous body pressure monitoring is required for areas where pressure ulcers are most likely to occur, including the sacrum, heel, ischium, ankle, and elbow.^[21] According to a previous report,^[22] 38.8% of pressure ulcers occur on the heel (29.7%) and the ankle (9.1%) of bed-ridden patients. Therefore, monitoring the pressure of the foot, which is particularly susceptible to pressure ulcers, is an effective preventative strategy.

Here, we demonstrate a wireless wearable heel pressure monitoring system that employs our proposed sensor. Three

3D-BLiPSs were attached to the sock of a subject to measure the pressure applied to the heel (S#1 and S#2) and the ankle (S#3) when lying down. The area of the heel that experiences pressure varies as the angle of the foot changes, and thus two sensors were attached to the heel (S#1) and the side of the heel (S#2), respectively (Figure 5a). In addition, when lying in a lateral position, the ankle contacts the floor; thus, its pressure was measured by S#3. In addition, a wireless communication system was implemented to remotely monitor the pressure sensor signals and to prevent electrical wires from restricting natural body movements (Figure 5b and Figure S10a,b, Supporting Information). In evaluating the pressure applied to the heel, we defined four lying positions: neutral (posture I: both toes pointing upward), leg-up (posture II: left leg raised), relaxed (posture III: both legs externally rotated), and lateral (posture IV: lying on the side). We also assessed three floor

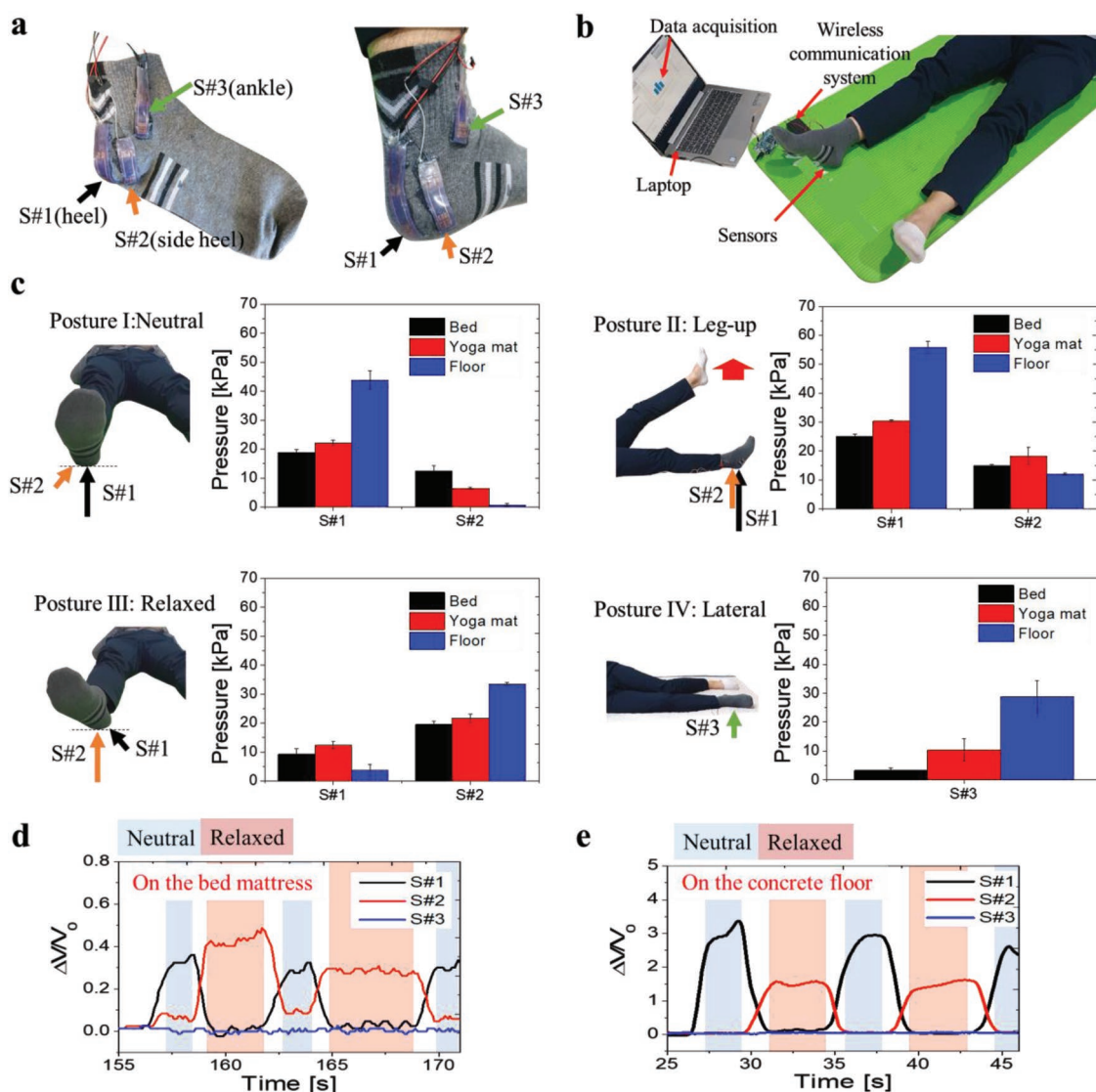


Figure 5. Health monitoring application of the 3D-BLiPS 2): Wireless heel pressure monitoring system. a) Three pressure sensors attached to the sock (S#1: heel; S#2: side heel; and S#3: ankle). b) Image of the measurement setup. c) Measurement data for the pressure on the sensors for different lying positions of the subject; posture I: neutral (toes pointed upward), posture II: leg-up, posture III: relaxed, and posture IV: lateral. d,e) Real-time response data for repeated position changes between posture I and III on a bed mattress and on a concrete floor.

conditions that differed by softness: a bed mattress (soft), a yoga mat (medium), and a concrete floor (hard; Figure S10c, Supporting Information).

In the neutral state (posture I), the pressure on S#1, located on the center of the heel, was the highest and that of S#2, located on the side of the heel, was relatively low. In particular, when lying on the concrete floor, the pressure was concentrated solely on S#1 ($\approx 43.7 \pm 3.3$ kPa), while almost no pressure was applied on S#2 ($\approx 0.7 \pm 0.6$ kPa). When lying on the bed mattress, however, the pressure on S#1 decreased to 18.8 ± 1.0 kPa. The pressure was well distributed across a larger contact area when lying on the bed, resulting in a lower maximum pressure on S#1 and a higher pressure on S#2 compared to other floor conditions. It can be seen that for more dynamic motion, such as the leg-up position (posture II), more pressure was applied on both S#1 and S#2 than in a neutral state (posture I). Because the right foot had to push on the floor to lift the left leg, a maximum pressure of 55.8 ± 2.1 kPa was applied to the right heel on the concrete floor. For the bed mattress and yoga mat, the pressure on the right heel increased compared to posture I by 5 and 8 kPa, respectively. In posture III, the leg rotates externally, and the main contact area changes from S#1 to S#2 as the angle of the foot changes. As a consequence, the pressure decreased on S#1 and increased on S#2. These changes were more significant on the concrete floor than on the bed mattress or yoga mat. In posture IV, the ankle touched the floor and an increase in pressure was measured for S#3. Because the ankle is a bony prominence like the heel, significant pressure is generated on the concrete floor ($\approx 28.8 \pm 5.6$ kPa). For the bed mattress, the larger contact area led to lower pressure ($\approx 3.2 \pm 1.0$ kPa) on the ankle.

We also repeatedly changed position between postures I and III and compared the dynamic signal changes for S#1–3 (Figure 5d,e). As the angle of the foot changed, the pressure at S#1 and S#2 alternated between increasing and decreasing directions (Video S1, Supporting Information), while the signal at S#3 remained at zero throughout the test. When taking the measurements on the bed mattress, it was observed that the signal at S#2 increased slightly for posture I, indicating that the pressure was dispersed on the heel compared to the concrete floor. In summary, the proposed body pressure monitoring system was able to measure the pressure applied to the heel and the ankle in both a static and a dynamic state, allowing the pressure distribution on the foot to be analyzed for various lying postures. By monitoring the pressures applied on the body parts, it is expected to be used as a wearable healthcare system for the prevention of pressure sores that can occur lying on the bed or wearing a prosthesis for a long time.

3. Conclusion

In this paper, a 3D-BLiPS was developed. By integrating a 3D-printed rigid microbump array with the liquid metal microchannel, the proposed pressure sensor has an extremely low detection limit (≈ 16 Pa) and an improved pressure sensitivity in low pressure range (0.158 kPa^{-1} @ 50 kPa) compared to previously reported liquid metal-based pressure sensors. Also, the negligible drift over 10 000 cycles, a large signal-to-noise ratio,

and excellent stability are advantageous over the characteristics of conventional solid-state pressure sensors. It achieved nearly perfect signal recovery after various forms of cyclic mechanical deformation, such as stretching and bending and negligible responds to environmental effects. We also demonstrated its use in two health monitoring applications: 1) a wearable wristband device that can continuously monitor the pulse during exercise and be employed in a noninvasive cuffless BP monitoring system based on PTT calculations, and 2) a wireless wearable heel pressure monitoring system that integrates three 3D-BLiPS with a wireless communication module. In the latter application, we successfully monitored heel pressure for various body positions and floor types, which can provide valuable information for bedridden patients to prevent pressure ulcers. As demonstrated in the study, the 3D-BLiPS could be utilized as a stand-alone device or within a multiarray device for the continuous monitoring of biosignals and body pressure with wireless communication systems as promising health monitoring applications. Opportunities for future research include the development of a whole-body pressure monitoring system related to other physical parameters (e.g., temperature, humidity, etc.) to gather more valuable information from patients. In addition, although not analyzed in the present study, the proposed pressure sensor shows significant potential for use in electronic skin and soft robotics, as well as various other health monitoring applications.

4. Experimental Section

Materials: PVA filament (2.75 mm, Ultimaker, USA), PLA filament (2.75 mm, Ultimaker, USA), Dragon Skin 10 (Smooth-on, USA), Galinstan (Santech Materials, China), and Easy Release 200 (Smooth-on, USA) were all used as purchased.

Preparation of the 3D-Printed Mold: The molds for microchannel fabrication and microbump array integration were designed with a 3D computer-aided design (CAD) program (Fusion 360, Autodesk, USA). The width and the height of the microchannel and the microbump were designed as $400 \mu\text{m} \times 200 \mu\text{m}$ and $400 \mu\text{m} \times 400 \mu\text{m}$, respectively. After modeling, the 3D CAD files were converted to stereolithography (STL) files for 3D printing and imported into 3D printing software (Cura 3.2, Ultimaker, USA). PVA and PLA filaments were allocated to each component, and 3D models were monolithically 3D-printed under customized printing conditions (e.g., nozzle temperature, printing bed temperature, etc.) using a commercial FDM 3D printer (Ultimaker 3, Ultimaker, USA) with a multiextrusion system. The actual dimension of the fabricated microchannel was $482 \pm 36 \mu\text{m}$ in width and $182 \pm 14 \mu\text{m}$ in height. Also, the fabricated microbump had a dimension of $477 \pm 46 \mu\text{m}$ in width and $339 \pm 13 \mu\text{m}$ in height (number of samples = 10). After printing, the master molds were carefully detached from the printing bed. The electric wires were attached at the ends of the mold using a temperature-adjustable soldering iron (Figure S2a–f, Supporting Information).

Fabrication of the 3D-BLiPS: Before spin-coating, a release agent was coated on a glass wafer to facilitate the release of the elastomer. A prepolymer mixture of Dragon Skin 10 was prepared by mixing its components A and B at a weight ratio of 1:1, after which it was spin-coated (400 rpm, 60 s) onto the prepared wafer as the bottom layer, followed by degassing in a vacuum chamber and curing at $60 \text{ }^\circ\text{C}$ for 2 h. The microchannel master molds were then put on the bottom layer and additional prepolymer was spin-coated (250 rpm, 60 s) as the top layer, followed by degassing. After curing, small holes were generated on the top layer at the ends of the molds for PVA removal. After 4 h of sonication in deionized water at $60 \text{ }^\circ\text{C}$ and repeated water intrusion

into the channel using a syringe, an empty microchannel with a rigid microbump array embedded above the channel was fabricated. The fabricated microchannel was filled with Galinstan using vacuum-filling^[23] or a syringe. In the final step, the holes were sealed with additional elastomer (Figure S2g–i, Supporting Information). The total thickness of the sensor was 1.01 ± 0.05 mm and the initial resistance was $0.41 \pm 0.05 \Omega$ ($n = 7$).

Sensor Characterization: Continuous pressure was applied using a universal testing machine (AG-X plus, Shimadzu, Japan) for full loading-unloading cycles. To apply the pressure on the pressure-sensing area of the sensor, an acryl cube with a contact area of 10×10 mm was placed on the sensor (Figure S4b, Supporting Information). The pressure was applied with a loading speed of 0.3 mm min^{-1} , while the corresponding resistance was measured using a source meter (Keithley 2400, Tektronix, USA) with Kelvin (4-wire) resistance measurement. Water droplets were dropped onto the pressure sensor using a disposable spoid and removed with the gentle use of a dry wiper. To measure the response time and the cyclic response of the sensor, a microactuator (MA-35, Physik Instrumente, Germany) and a force transducer (SM-500N, Interface, USA) were used under displacement control loading conditions. For the cyclic loading of longitudinal strain and bending, a linear stage with a source meter (Figure S4c–e, Supporting Information) was implemented. To test the thermal stability, an aluminum plate with the sensor and a thermocouple (HH147, Omega Engineering, USA) used as a temperature reference was attached to a hot plate and the temperature of the sensor was controlled by adjusting the temperature of the hot plate. For moisture sensitivity testing, the 3D-BLiPS was immersed in deionized water for 4 weeks and its base resistance was measured every week.

Epidermal Pulse-Monitoring Wristband and Cuffless Blood Pressure Estimation System: The 3D-BLiPS was attached to a wristband with a 3D-printed half-cylindrical support. The support ensured a firm contact between the skin and the sensor when wearing the wristband. The sensor and the reference resistors were connected in series for a voltage dividing circuit (Figure S9a, Supporting Information). The 9mplied signal was recorded by an Arduino Due (Arduino.cc) with a 12-bit resolution (Figure S9b, Supporting Information). To detect the ECG signals, a commercial ECG sensor (PSL-iECG2, Physioblab, Korea) compatible with the Arduino board was utilized (Figure S9c, Supporting Information). Subject A (28, male, 65 kg) and Subject B (27, male, 85 kg) completed 45 full squats in 45 s wearing the epidermal pulse-monitoring wristband. After exercise, the subjects sat on a chair and rested for 5 min. With the raw data, their pulse was plotted in bpm over time by calculating the number of peaks in 10 s intervals using MATLAB (MATLAB 2018, Mathworks Inc., USA), followed by a data-smoothing process (6 points of Savitzky–Golay method using OriginPro 8.5). To measure the ECG signal for the PTT calculation, additional three electrodes were attached to the arms of Subject A. Red (In+) and white (Reference) electrodes were attached to the left arm and black (In-) electrodes were attached to the right arm. The ECG and pulse signals were measured simultaneously and the pulse signals were smoothed with 20 points using Savitzky–Golay method. To estimate the blood pressure, PTTs for each pulse were calculated in 5 s interval for both before the exercise ($n = 7$) and after the exercise ($n = 12$). For comparison, SBP and DBP before and after exercise were measured using an automatic digital blood pressure monitor (BP170, Inbody, Korea). The data and equations used for estimating the blood pressure are summarized in Table S1 (Supporting Information).^[17a,18a]

Wireless Wearable Heel Pressure Monitoring System: Three 3D-BLiPSs were attached to a sock: one on the heel (S#1), one on the side of the heel (S#2), and one on the ankle (S#3). The sensors were directly adhered to the sock using a fast-curing elastomer, while the sock was being worn. Voltage dividing circuits were built for each pressure sensor and connected to the Arduino Due for analog-to-digital conversion (ADC). To increase the ADC resolution, an external analog reference were used by supplying 1.6 V to the board with a 12-bit resolution. Commercial Bluetooth modules (HC-06) were also integrated into the circuits for wireless communication. The output voltages of the pressure sensor in the integrated device system was acquired with a sampling

frequency of 20 Hz. The acquired ADC data were plotted in real-time using MATLAB with a moving average of 20 points. The pressure was calculated using calibration functions in MATLAB, which were derived from the pressure sensing characterization data. A constant parasitic resistance of the interconnections among the electrical wires in the integrated device system were compensated for accurate pressure calibration. The means and standard deviations of the representative pressure values were calculated from the maximum pressures of each repetitive loading ($n = 5$) with different lying postures. All experiments on human skin were carried out under approval from coauthors of the paper. The experiments were conducted with informed signed consent from the subjects. According to the standard, formal approval for this study from the university authorities was not required.

Supporting Information

Supporting Information is available from the Wiley Online Library or from the author.

Acknowledgements

This work was supported by a National Research Foundation of Korea (NRF) grant funded by the Korean government (MSIT) (No. 2018R1A2B2004910) and a National Research Foundation of Korea (NRF) Grant funded by the Korean government (MSIP) (No. 2015R1A5A1037668).

Conflict of Interest

The authors declare no conflict of interest.

Keywords

3D printing, health monitoring, liquid metal, pressure sensors, wearable sensors

Received: July 23, 2019

Revised: September 20, 2019

Published online: October 9, 2019

- [1] a) Z. Lou, S. Chen, L. Wang, K. Jiang, G. Shen, *Nano Energy* **2016**, 23, 7; b) H. Tian, Y. Shu, X.-F. Wang, M. A. Mohammad, Z. Bie, Q.-Y. Xie, C. Li, W.-T. Mi, Y. Yang, T.-L. Ren, *Sci. Rep.* **2015**, 5, 8603.
- [2] a) S.-J. Woo, J.-H. Kong, D.-G. Kim, J.-M. Kim, *J. Mater. Chem. C* **2014**, 2, 4415; b) D. Kwon, T.-I. Lee, J. Shim, S. Ryu, M. S. Kim, S. Kim, T.-S. Kim, I. Park, *ACS Appl. Mater. Interfaces* **2016**, 8, 16922; c) K. Kim, J. Park, J.-h. Suh, M. Kim, Y. Jeong, I. Park, *Sens. Actuators, A* **2017**, 263, 493; d) S. Kim, M. Amjadi, T.-I. Lee, Y. Jeong, D. Kwon, M. S. Kim, K. Kim, T.-S. Kim, Y. S. Oh, I. Park, *ACS Appl. Mater. Interfaces* **2019**, 11, 23639.
- [3] X. Wu, Y. Han, X. Zhang, Z. Zhou, C. Lu, *Adv. Funct. Mater.* **2016**, 26, 6246.
- [4] a) Z. Wang, S. Wang, J. Zeng, X. Ren, A. J. Chee, B. Y. Yiu, W. C. Chung, Y. Yang, A. C. Yu, R. C. Roberts, *Small* **2016**, 12, 3827; b) S. R. A. Ruth, L. Beker, H. Tran, V. R. Feig, N. Matsuhisa, Z. Bao, *Adv. Funct. Mater.* **2019**, 1903100; c) M. S. Kim, D. Kwon, S. Kim, K. Kim, I. Park, presented at 2017 IEEE 30th International Conference on Micro Electro Mechanical Systems (MEMS), Las Vegas, NV, USA, January **2017**.

- [5] a) D. Y. Choi, M. H. Kim, Y. S. Oh, S.-H. Jung, J. H. Jung, H. J. Sung, H. W. Lee, H. M. Lee, *ACS Appl. Mater. Interfaces* **2017**, *9*, 1770; b) J.-B. Chossat, Y.-L. Park, R. J. Wood, V. Duchaine, *IEEE Sens. J.* **2013**, *13*, 3405.
- [6] a) M.-F. Lin, J. Xiong, J. Wang, K. Parida, P. S. Lee, *Nano Energy* **2018**, *44*, 248; b) S. Xu, D. M. Vogt, W. H. Hsu, J. Osborne, T. Walsh, J. R. Foster, S. K. Sullivan, V. C. Smith, A. W. Rousing, E. C. Goldfield, *Adv. Funct. Mater.* **2019**, *29*, 1807058; c) Y. J. Gao, H. Ota, E. W. Schaler, K. Chen, A. Zhao, W. Gao, H. M. Fahad, Y. G. Leng, A. Z. Zheng, F. R. Xiong, C. C. Zhang, L. C. Tai, P. D. Zhao, R. S. Fearing, A. Javey, *Adv. Mater.* **2017**, *29*, 1701985; d) S. G. Yoon, S. T. Chang, *J. Mater. Chem. C* **2017**, *5*, 1910.
- [7] a) M. D. Dickey, *Adv. Mater.* **2017**, *29*, 1606425; b) E. Palleau, S. Reece, S. C. Desai, M. E. Smith, M. D. Dickey, *Adv. Mater.* **2013**, *25*, 1589; c) R. Matsuzaki, K. Tabayashi, *Adv. Funct. Mater.* **2015**, *25*, 3806.
- [8] a) R. D. P. Wong, J. D. Posner, V. J. Santos, *Sens. Actuators, A* **2012**, *179*, 62; b) C. B. Cooper, K. Arutselvan, Y. Liu, D. Armstrong, Y. Lin, M. R. Khan, J. Genzer, M. D. Dickey, *Adv. Funct. Mater.* **2017**, *27*, 1605630.
- [9] a) H.-S. Shin, J. Ryu, C. Majidi, Y.-L. Park, *J. Micromech. Microeng.* **2016**, *26*, 025011; b) H.-S. Shin, Y.-L. Park, presented at the IEEE SENSORS 2014 Conf., Valencia, Spain, November **2014**.
- [10] a) T. Jung, S. Yang, *Sensors* **2015**, *15*, 11823; b) M. g. Kim, H. Alrowais, O. Brand, *Adv. Electron. Mater.* **2018**, *4*, 1700434; c) J. C. Yeo, J. Yu, K. P. Loh, Z. Wang, C. T. Lim, *ACS Sens.* **2016**, *1*, 543; d) J. C. Yeo, J. Yu, Z. M. Koh, Z. Wang, C. T. Lim, *Lab Chip* **2016**, *16*, 3244.
- [11] a) Y.-L. Park, B.-R. Chen, R. J. Wood, *IEEE Sens. J.* **2012**, *12*, 2711; b) A. Anderson, Y. Mengüç, R. J. Wood, D. Newman, *IEEE Sens. J.* **2015**, *15*, 6229.
- [12] Y. Gao, H. Ota, E. W. Schaler, K. Chen, A. Zhao, W. Gao, H. M. Fahad, Y. Leng, A. Zheng, F. Xiong, *Adv. Mater.* **2017**, *29*, 1701985.
- [13] a) Y.-L. Park, C. Majidi, R. Kramer, P. Bérard, R. J. Wood, *J. Micromech. Microeng.* **2010**, *20*, 125029; b) Y.-L. Park, D. Tepayotl-Ramirez, R. J. Wood, C. Majidi, *Appl. Phys. Lett.* **2012**, *101*, 191904.
- [14] a) E. Roh, H. B. Lee, D. I. Kim, N. E. Lee, *Adv. Mater.* **2017**, *29*, 1703004; b) S. Jang, C. Kim, J. J. Park, M. L. Jin, S. J. Kim, O. O. Park, T. S. Kim, H. T. Jung, *Small* **2018**, *14*, 1702818; c) K. Kim, J. Choi, Y. Jeong, M. Kim, I. Cho, S. Kim, Y. Oh, I. Park, presented at 2019 20th International Conference on Solid-State Sensors, Actuators and Microsystems & Eurosensors XXXIII (TRANSDUCERS & EUROSENSORS XXXIII), Berlin, Germany, June **2019**.
- [15] a) X. Ding, B. P. Yan, Y.-T. Zhang, J. Liu, N. Zhao, H. K. Tsang, *Sci. Rep.* **2017**, *7*, 11554; b) R. Mukkamala, J.-O. Hahn, O. T. Inan, L. K. Mestha, C.-S. Kim, H. Töreyn, S. Kyal, *IEEE Trans. Biomed. Eng.* **2015**, *62*, 1879.
- [16] a) M. Kachuee, M. M. Kiani, H. Mohammadzade, M. Shabany, *IEEE Trans. Biomed. Eng.* **2017**, *64*, 859; b) K. Matsumura, P. Rolfe, S. Toda, T. Yamakoshi, *Sci. Rep.* **2018**, *8*, 7298.
- [17] a) N. Luo, W. Dai, C. Li, Z. Zhou, L. Lu, C. C. Poon, S. C. Chen, Y. Zhang, N. Zhao, *Adv. Funct. Mater.* **2016**, *26*, 1178; b) K. Meng, J. Chen, X. Li, Y. Wu, W. Fan, Z. Zhou, Q. He, X. Wang, X. Fan, Y. Zhang, *Adv. Funct. Mater.* **2019**, *29*, 1806388.
- [18] a) C. Poon, Y. Zhang, presented at 2005 IEEE Engineering in Medicine and biology 27th Annual Conference, Shanghai, China, September **2005**; b) Y. Zheng, C. C. Poon, B. P. Yan, J. Y. Lau, *J. Med. Syst.* **2016**, *40*, 195.
- [19] a) C. Gerlach, D. Krumm, M. Illing, J. Lange, O. Kanoun, S. Odenwald, A. Hübler, *IEEE Sens. J.* **2015**, *15*, 3647; b) J. McNeill, D. Sen, Y. Mendelson, M. Crivello, S. Mazumder, A. Agdeppa, S. A. Hussein, H. Kim, V. Loehle, R. Dunn, presented at 2017 IEEE International Symposium on Circuits and Systems (ISCAS), Baltimore, MD, USA, May **2017**; c) S. Han, J. Kim, S. M. Won, Y. Ma, D. Kang, Z. Xie, K.-T. Lee, H. U. Chung, A. Banks, S. Min, *Sci. Transl. Med.* **2018**, *10*, eaan4950.
- [20] a) P. K. Vadivu, *Indian J. Surg.* **2015**, *77*, 576; b) J. E. Sanders, B. S. Goldstein, D. F. Leotta, *J. Rehabil. Res. Dev.* **1995**, *32*, 214.
- [21] a) D. Bluestein, A. Javaheri, *Am. Fam. Physician* **2008**, *78*, 1186; b) S. A. Shah, N. Zhao, A. Ren, Z. Zhang, X. Yang, J. Yang, W. Zhao, *IEEE Access* **2016**, *4*, 8065;
- [22] a) M. Clark, G. Bours, T. Defloor, *EPUAP Rev.* **2002**, *4*, 49; b) M. Romanelli, M. Clark, A. Gefen, G. Ciprandi, *Science and Practice of Pressure Ulcer Management*, Springer, London **2006**.
- [23] Y. Lin, O. Gordon, M. R. Khan, N. Vasquez, J. Genzer, M. D. Dickey, *Lab Chip* **2017**, *17*, 3043.